Calibrating surface hyperelastic constitutive models in soft solids

M. Rashid Zafar* and Sumit Basu†
Department of Mechanical Engineering, IIT Kanpur, Kanpur 208016, Uttar Pradesh, India

(Received 24 February 2021; revised 3 May 2021; accepted 25 May 2021; published 14 June 2021)

Soft solids such as silicone gels, with bulk shear modulus ranging from ∼10 to 1000 kPa, exhibit strongly strain-dependent surface stresses. Moreover, unlike conventional stiffer materials, the effects of surface stress in these materials manifest at length scales of tens of micrometers rather than nanometers. However, the calibration of constitutive parameters for surface hyperelasticity has proved to be challenging. Using a reasonably general surface constitutive model, we explore the possibility of obtaining its parameters from force-twist, torque-twist, and force-extension (force-compression) responses of a soft cylinder held between two inert, rigid plates. The motivation behind using these responses is derived from the fact that the roles of the surface constitutive parameters, under suitably ideal conditions, are neatly separated from each other and the three responses easily yield values of the three parameters. Moreover, through large deformation finite-element simulations with coupled bulk and surface hyperelasticity, we delineate the extent to which deviation from the ideal conditions may be tolerated. Using an example with previously reported material parameters, we estimate that, for cylindrical specimens with a radius of the order of 100 μm, the capability to measure forces and torques of the order of 1–100 μN and 10^3–10^5 μN-μm, respectively, will be required to determine the parameters accurately.

DOI: 10.1103/PhysRevE.103.063003

I. INTRODUCTION

Surface tension in liquids is isotropic, deformation independent, and numerically equal to the liquid's surface free energy. In analogy with surface tension, surface stresses in solids can also be envisaged [1]. However, solid surface stress is, in general, anisotropic and deformation dependent and is related to the surface energy by the Shuttleworth equation [2]. In a deforming solid, strain energy is apportioned into that of the bulk and the bounding surface, which obey different constitutive formulations. In the case of stiff, crystalline solids, surface stresses are negligible at the macroscale and become important only at the nanoscale (see, e.g., Refs. [3–5]).

Broadly speaking, surface elasticity assumes importance at length scales comparable to the so-called elastocapillary length given by γ/E, where γ and E are measures (surface tension and bulk shear modulus, for instance) characterizing the elasticity of the surface and the bulk, respectively. Ultrasoft solids such as silicone gels and hydrogels have bulk moduli ranging from 100 Pa to 100 kPa. Reported values of the surface tension of silicone gels are in the range of 20–100 mN/m [6–10], leading to elastocapillary lengths of ∼10–200 μm. At length scales of hundreds of micrometers, contrary to stiff crystalline materials, surface elasticity assumes importance in the case of these ultrasoft solids.

Soft solids are increasingly being used in applications ranging from orthopedic implants [11,12], tissue engineering [13], electronic packaging [14], to soft robotics [13]. Moreover, the effects of surface elasticity in these materials are not subtle. Surface elasticity significantly affects the geometry close to the contact line between soft solid spheres and a rigid surface [15] as well as between a soft solid surface and a liquid droplet [6,16,17]. The depth sensing indentation response of soft solid surfaces is also influenced by surface elasticity [18]. It also competes with the elasticity of the bulk to produce longitudinal undulations on thin soft filaments [19] and controls the wavelength of instability patterns in thin, soft, confined films [20].

To model and understand many of the above phenomena, a complete constitutive characterization of both the bulk and surface elastic responses is necessary. However, the constitutive behavior of the surface in a soft solid can be difficult to calibrate through experiments. If we assume that the surface stress is independent of surface strains, the problem becomes somewhat tractable and ingenious albeit indirect methods have been used to measure surface stress in such cases. For instance, Nadermann *et al.* [7] have measured surface stresses in a soft solid film by placing a drop under the film. Mondal *et al.* [9] have estimated the surface tension of an elastomer by monitoring the deformation of the surface when a liquid is forced into a cylindrical channel located right below the surface. Xu *et al.* [10] indented thin films of a relatively stiff solid (Young's modulus ≃100 kPa) to measure surface stresses. Assuming the surface stress to be independent of surface strains results in a wide scatter in the values determined by these studies. For example, reported values of the surface tension of silicone range from ∼20 to 100 mN/m [6–10].

When the surface stress depends on surface strains, the experimental characterization of the surface constitutive behavior becomes more challenging (e.g., Ref. [16]). In general, the energy per unit undeformed area γ of an elastic surface

*rashidzafar@zhcet.ac.in; also at Department of Mechanical Engineering, ZHCET, AMU, Aligarh, UP-202002, India.
†Corresponding author: sbasu@iitk.ac.in

has an isotropic part and a part dependent on surface strains [21]. One method of characterizing surface constitutive behavior involves concentrating on the microscopic structure of the wetting profile at the contact line between vapor, a liquid droplet, and a prestretched flat soft solid. In this region, locally, strain energetic contributions from the surface outweigh that from the bulk. In fact, Xu *et al.* [22] characterized both the strain-independent and strain-dependent parts of the surface stress using the geometry of the wetting ridge formed at the contact line of a stretched silicon gel substrate with a liquid droplet. Xu *et al.* [22] assumed that the surface stress depends linearly on the surface strain, and showed surface stress increases very significantly over its initial value with deformation. Their results unequivocally establish that strain-dependent surface stresses in soft materials are an essential aspect of their constitutive behavior.

In this paper we propose a more direct method for characterizing the surface constitutive behavior. The elastic parameters of macroscopic, stiffer engineering materials are routinely obtained from tests where reasonably homogeneous states of uniaxial (or, at most, biaxial) stress are established in the test specimen. These tests are useful because the experimentally measurable force-displacement (or torque-twist) response of the sample can be easily connected to the uniaxial stress strain behavior. We explore the possibility of extracting surface elasticity parameters in soft solids through such direct tests.

The above approach allows us to calibrate a more versatile surface stress–surface strain relationship than has been attempted so far. At the very least, surface stresses can arise due to stretch in either principal direction or change in surface area. Specifically, as an alternative to indirect tests (e.g., characterizing elasticity parameters by studying the geometric properties of the wetting ridge), we propose that surface elasticity in soft solids can also be characterized using "global" force-displacement or torque-twist responses of soft solid samples. In particular, we show that theoretically, under reasonable simplifying assumptions, it is possible to partition the axial force and torque in a sequence of tension (compression) and twisting protocols on soft cylinders in a manner such that the characteristic parameters of the surface elastic constitutive equation are easily determined.

The idea is further explained in Figs. 1(a)–1(c). A soft cylinder of radius R_0 and length L is molded in a rigid mold between two plates at $Z = 0$ and L. The lower plate is fixed. Force F_z and torque M_z exerted on the upper plate are measured. The stretch of the cylinder in the Z direction is denoted by λ and is the ratio between the deformed length and reference length L. As soon as the mold is removed [Fig. 1(b)], the cylinder exerts a force on the upper plate, $F_z(\lambda = 1)$. The cylinder is subsequently extended (compressed) to λ and twisted by τL with a torque M_z (with the twist per unit undeformed length being denoted by τ) as shown in Fig. 1(c). We show that as the cylinder is subjected to a combined tension (compression) and torsion, the axial force $F_z(\lambda, \tau)$ and torque $M_z(\lambda, \tau)$ can be partitioned neatly into parts that depend on the bulk and surface hyperelastic properties.

However, in order to extract the surface hyperelastic parameters, the cylindrical specimen must be small, probably in the micrometer range. Measuring forces and torques will also require sensitive devices. While we do not attempt an implementation of the idea, a few practical aspects need attention. These are elucidated through large deformation-based finite-element (FE) simulations with coupled bulk and surface hyperelasticity.

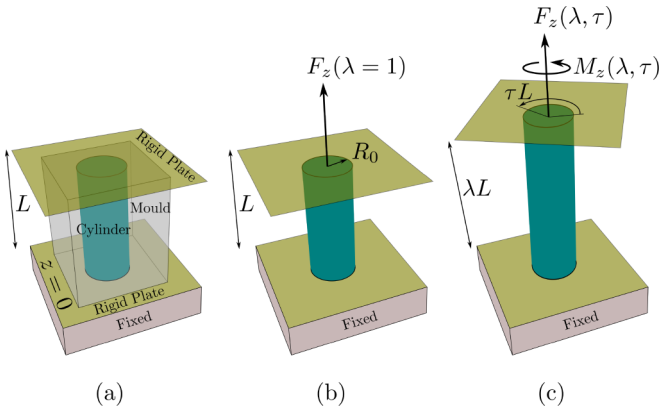

FIG. 1. We consider that a soft solid is held in a rigid mold in (a) and the mold is removed in (b). The cylinder has an initial radius R_0 while it is held between two rigid plates. In (c) the axial force and torque, F_z and M_z, respectively, are measured on the upper plate while the cylinder is extended (compressed) and twisted, while the lower plate is held fixed. The initial length of the cylinder is L.

Four possible deviations from the ideal conditions assumed in deriving the closed-form solutions are considered. First, fidelity to the closed-form solutions for F_z and M_z will depend on the aspect ratio L/R_0. Second, it will also depend on whether or not the bulk is perfectly incompressible. Third, whether the sample sticks to the upper plate or slips on it is expected to affect the overall F_z or M_z. Finally, when removed from the mold, a soft solid may deviate from cylindricity depending on its length and surface energies of the plate and surrounding fluid. We study the effects of each of these possibilities with a view to suggest approximate limits on the specimen sizes that will allow us to effectively determine the surface characterizing parameters.

II. A SOFT CYLINDER UNDER COMBINED TENSION (COMPRESSION) AND TORSION

The kinematics and kinetics of a solid undergoing large deformations within the framework of coupled bulk and surface hyperelasticity have been discussed by many authors (e.g., Refs. [23–27]). Details of the continuum mechanics formulation and FE implementation are also given in our earlier work [28].

Consider the undeformed and deformed configurations of a cylinder under combined extension (compression) and torsion, shown in Fig. 2. Both the undeformed and deformed configurations are axisymmetric. We use the cylindrical polar coordinate systems with base vectors $\boldsymbol{E}_R, \boldsymbol{E}_\Theta, \boldsymbol{E}_Z$ and $\boldsymbol{e}_r, \boldsymbol{e}_\theta, \boldsymbol{e}_z$ to describe a position in reference and current configurations, respectively. The surface of the cylinder in reference and current configurations is spanned by $\boldsymbol{E}_\Theta, \boldsymbol{E}_Z$ and $\boldsymbol{e}_\theta, \boldsymbol{e}_z$, respectively.

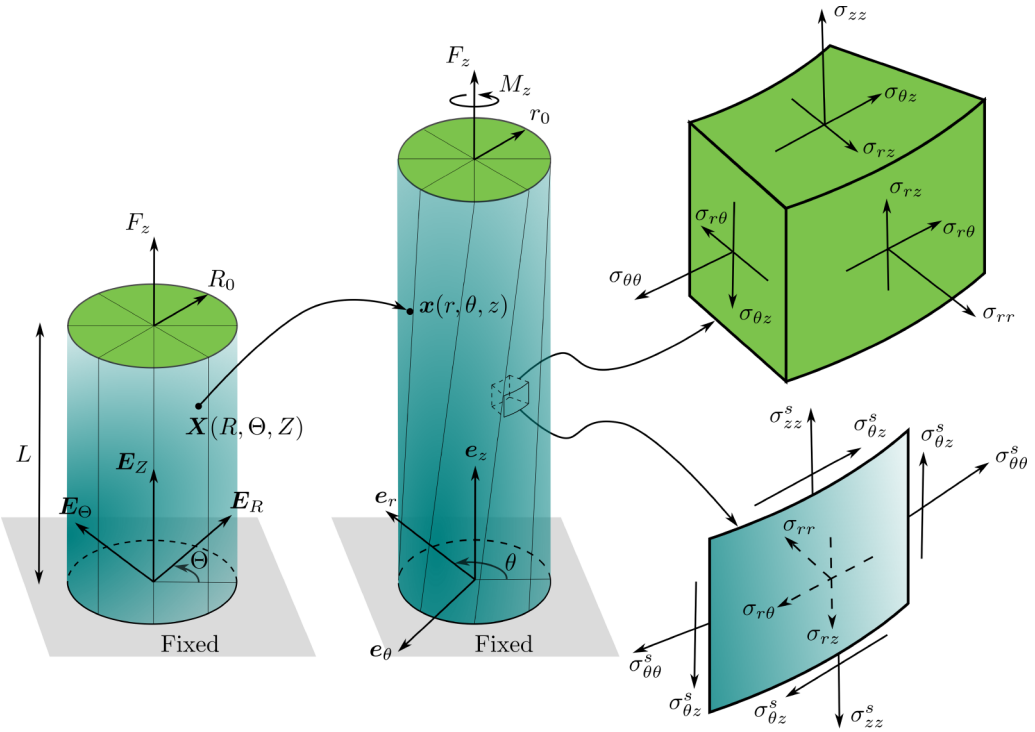

FIG. 2. The initial configuration of the cylinder of radius R_0 and length L is deformed into a twisted and extended (compressed) final configuration. The coordinates of a point are (R, Θ, Z) in the initial configuration and it maps, under twist and extension (compression), to (r, θ, z) in the deformed one. The Cauchy stress in an infinitesimal element in the bulk as well as the coupling between bulk and surface stresses at $r = r_0$ are also shown.

In the bulk, the Cauchy stress $\boldsymbol{\sigma}$, in the absence of body forces, is governed by the equilibrium equation

$$\operatorname{div} \boldsymbol{\sigma} = \boldsymbol{0}, \tag{1}$$

where $\operatorname{div}(\cdot)$ is obtained with respect to current coordinates. The bulk Cauchy stress is obtained from an isotropic strain energy density function W, that, for an incompressible bulk, depends on the first two invariants I_1 and I_2 of the right Cauchy-Green strain tensor $\boldsymbol{C}$.

The surface of the solid is like an infinitesimally thin but stretchable "wrapper" attached to the bulk. It is also endowed with a separate constitutive equation. The strain energy density (energy per unit undeformed surface area) γ of the surface depends on the invariants of the surface right Cauchy strain tensor $\boldsymbol{C}^s$, i.e., I^s_1 and I^s_2. Surface Cauchy stress $\boldsymbol{\sigma}^s$, shown in Fig. 2, is obtained in terms of the derivatives of $\gamma(I^s_1, I^s_2)$. On the surface at $r = r_0$, where the outward normal is $\boldsymbol{e}_r$, equilibrium demands that

$$\operatorname{div}^s \boldsymbol{\sigma}^s|_{r_0} = (\boldsymbol{\sigma} \cdot \boldsymbol{e}_r)|_{r_0}. \tag{2}$$

The right-hand side represents the traction due to the bulk stress $\boldsymbol{\sigma}$ and, if surface elasticity was negligible, for a traction-free surface, it would have been zero. In our case, the surface divergence of $\boldsymbol{\sigma}^s$ balances the traction due to the bulk stress $\boldsymbol{\sigma}$ at the surface $r = r_0$.

Consider a combined extension (compression) and torsion of the undeformed cylinder occupying the volume $0 \leqslant R \leqslant R_0$, $0 \leqslant \Theta < 2\pi$, $0 \leqslant Z \leqslant L$. As shown in Fig. 2, a generic point $\boldsymbol{X}$ (defined by coordinates R, Θ, Z) is mapped to $\boldsymbol{x}$ (defined by r, θ, z) as

$$\begin{aligned} r &= \lambda^{-1/2} R, \\ \theta &= \Theta + \tau Z, \\ z &= \lambda Z. \end{aligned} \tag{3}$$

The axial extension (compression) is characterized by λ, while τ is the twist per unit undeformed length. Note that λ and τ do not vary spatially. Also, the cylinder is assumed to remain a cylinder throughout the deformation.

The bulk Cauchy stress tensor in matrix notation can be written as (see Appendix B)

$$\boldsymbol{\sigma} = -p \begin{pmatrix} 1 & 0 & 0 \\ 0 & 1 & 0 \\ 0 & 0 & 1 \end{pmatrix} + 2W_1 \begin{pmatrix} \lambda^{-1} & 0 & 0 \\ 0 & \lambda^{-1} + \tau^2 r^2 & \lambda \tau r \\ 0 & \lambda \tau r & \lambda^2 \end{pmatrix} - 2W_2 \begin{pmatrix} \lambda & 0 & 0 \\ 0 & \lambda & -\tau r \\ 0 & -\tau r & \lambda^{-2} + \lambda^{-1} \tau^2 r^2 \end{pmatrix}, \tag{4}$$

where $W_1 = \frac{\partial W}{\partial I_1}$ and $W_2 = \frac{\partial W}{\partial I_2}$. The undetermined pressure $p(r, \theta, z)$ arises due to incompressibility. It can be shown to be a function of r only. As shown in Appendix A, it is determined from boundary conditions and the equilibrium equation as

$$p = -\int 2W_1 \tau^2 r dr + (2W_1 \lambda^{-1} - 2W_2 \lambda) + C, \tag{5}$$

where C is a constant of integration.

Similarly, using the referential surface strain energy density (which is a function of the invariants of the right

Cauchy-Green surface strain tensor $\boldsymbol{C}^s$, i.e., I_1^s, I_2^s), the Cauchy surface stress tensor can be obtained in a similar manner as (see Appendix B)

$$\boldsymbol{\sigma}^s = 2\gamma_1\lambda^{-1/2}\begin{pmatrix}\lambda^{-1}+\tau^2 r^2 & \lambda\tau r\\ \lambda\tau r & \lambda^2\end{pmatrix} + 2\gamma_2\lambda^{1/2}\begin{pmatrix}1 & 0\\ 0 & 1\end{pmatrix}, \tag{6}$$

where $\gamma_1 = \frac{\partial\gamma}{\partial I_1^s}$ and $\gamma_2 = \frac{\partial\gamma}{\partial I_2^s}$. Recall that the surface stress is $\boldsymbol{\sigma}^s = \sigma^s_{\theta\theta}\boldsymbol{e}_\theta\boldsymbol{e}_\theta + \sigma^s_{\theta z}\boldsymbol{e}_\theta\boldsymbol{e}_z + \sigma^s_{z\theta}\boldsymbol{e}_z\boldsymbol{e}_\theta + \sigma^s_{zz}\boldsymbol{e}_z\boldsymbol{e}_z$.

Equilibrium at the surface $r = r_0$ is governed by Eq. (2). This equation has to be used to determine the constant C in Eq. (5). The procedure for doing so involves computing the surface divergence of the surface stress $\boldsymbol{\sigma}^s$ and is detailed in Appendix C.

Now substituting Eq. (5) in Eq. (4), we can easily extract the axial stress component σ_{zz} as

$$\sigma_{zz} = \int 2W_1\tau^2 r dr + 2W_1(\lambda^2-\lambda^{-1}) - 2W_2(\lambda^{-2}-\lambda+\lambda^{-1}\tau^2 r^2) - C, \tag{7}$$

where the expression for C is to be taken from Eq. (C7).

The total axial force F_z and total axial moment M_z on the cylinder can be calculated as

$$F_z = F_z^b + F_z^s,$$
$$M_z = M_z^b + M_z^s,$$

where the axial forces due to bulk and surface stresses are evaluated as

$$F_z^b = \int_0^{2\pi}\int_0^{r_0}\sigma_{zz} r d\theta dr,$$

$$F_z^s = \int_0^{2\pi}\sigma^s_{zz} r_0 d\theta, \tag{8}$$

respectively. The contributions to the axial moment from the bulk and the surface stresses are

$$M_z^b = \int_0^{2\pi}\int_0^{r_0}\sigma_{\theta z} r^2 d\theta dr,$$

$$M_z^s = \int_0^{2\pi}\sigma^s_{\theta z} r_0^2 d\theta. \tag{9}$$

It will be shown in Sec. II A that the total force and moment can be decoupled in the sense that one part depends on the surface hyperelastic parameters while the other depends on the bulk. We can derive compact versions of these contributions for specific forms of W and γ and loading protocols.

A. Axial force and moment for specific forms of $W(I_1, I_2)$

We consider two specific forms of the bulk strain energy density $W(I_1, I_2)$, namely, the neo-Hookean with

$$W = \frac{\mu}{2}(I_1 - 3), \tag{10}$$

and Gent [29] with

$$W = -\frac{\mu J_m}{2}\log\left(1 - \frac{I_1 - 3}{J_m}\right). \tag{11}$$

In both the models, μ denotes the modulus of the hyperelastic bulk. The Gent model [29] phenomenologically accounts for the finite extensibility of macromolecular chains making up the underlying network, i.e., it models unbounded stiffening of the material as $I_1 \to J_m + 3$. It reduces to the neo-Hookean model [Eq. (10)] as $J_m \to \infty$.

For the surface, a minimal hyperelastic surface energy density function is chosen. This includes an initial surface stress that is independent of surface strains with further strain-dependent contributions dependent on I_1^s, I_2^s [21]. With such a model, we have three parameters σ_o, μ_s, and λ_s to be calibrated. The first parameter is akin to surface tension and contributes even in the absence of surface strains. The second includes the energetic cost of unidirectional stretching of the surface, while the third governs its response to purely areal stretches. Thus,

$$\gamma = \sigma_o\sqrt{I_2^s} + \frac{\mu_s}{2}\left(I_1^s - 2 - \log I_2^s\right) + \frac{\lambda_s}{8}\left(\log I_2^s\right)^2. \tag{12}$$

We will also use the following nondimensional quantities (denoted by an overbar):

$$\overline{F}_z = \frac{F_z}{\mu R_0^2},\quad \overline{M}_z = \frac{M_z}{\mu R_0^3},\quad \overline{W}_1 = \frac{W_1}{\mu},\quad \overline{W}_2 = \frac{W_2}{\mu},\quad \overline{R} = \frac{R}{R_0},\quad \overline{\tau} = \tau R_0,\quad \overline{\gamma}_1 = \frac{\gamma_1}{\mu R_0},\quad \overline{\gamma}_2 = \frac{\gamma_2}{\mu R_0}. \tag{13}$$

Here, R denotes the radial coordinate of a point in the undeformed configuration, which maps to r in the deformed. Consequently, R_0 maps to r_0. Note that the quantities associated with surface hyperelasticity, namely, γ_1, γ_2, are normalized by μR_0. So $\overline{\gamma}_\alpha$ (for $\alpha = 1, 2$) can be small, and the effect of surface hyperelasticity negligible, if the cylinder either has a large radius R_0 or its surface parameter γ_α is small. Surface effects are small also for materials with large modulus μ.

Extracting bulk and surface stress components from Eqs. (4) and (6), respectively, and substituting in Eqs. (8) and (9), we can derive the nondimensional axial force and moment as

$$\frac{\overline{F}_z}{\pi} = \underbrace{2\int_0^1\left(2\overline{W}_1(\lambda-\lambda^{-2}) - 2\overline{W}_2(\lambda^{-3}-\lambda^{-1}+\lambda^{-3}\overline{\tau}^2\overline{R}^2) - \int_{\overline{R}}^1 2\overline{W}_1\lambda^{-2}\overline{\tau}^2\overline{R}d\overline{R}\right)\overline{R}d\overline{R}}_{\text{bulk contribution}} + \underbrace{2\overline{\gamma}_1(2\lambda-\lambda^{-2}-\lambda^{-2}\overline{\tau}^2)+2\overline{\gamma}_2}_{\text{surface contribution}}, \tag{14}$$

$$\frac{\overline{M}_z}{\pi} = \underbrace{2\overline{\tau}\int_0^1 (2\overline{W}_1 + 2\overline{W}_2\lambda^{-1})\lambda^{-1}\overline{R}^3 d\overline{R}}_{\text{bulk contribution}} + \underbrace{4\overline{\gamma}_1\lambda^{-1}\overline{\tau}}_{\text{surface contribution}}. \tag{15}$$

It is obvious from Eqs. (14) and (15) that the contributions from bulk and surface energies are completely decoupled. When the bulk is neo-Hookean [Eq. (10)] and the surface obeys Eq. (12), the axial force and moment take the forms

$$\frac{\overline{F}_z}{\pi} = (\lambda - \lambda^{-2}) - \frac{1}{4}\lambda^{-2}\overline{\tau}^2 + \overline{\sigma}_o\lambda^{-1/2} + \overline{\mu}_s(2\lambda - \lambda^{-1} - \lambda^{-2} - \lambda^{-2}\overline{\tau}^2) + \frac{\overline{\lambda}_s}{2}\lambda^{-1}\log\lambda, \tag{16}$$

$$\frac{\overline{M}_z}{\pi} = \left(\frac{1}{2} + 2\overline{\mu}_s\right)\lambda^{-1}\overline{\tau}. \tag{17}$$

For a bulk that obeys the Gent model, these quantities are

$$\frac{\overline{F}_z}{\pi} = \frac{J_m(J_m - 3\lambda^2 + 3)}{2\overline{\tau}^2}\log\left(\frac{J_m - 2\lambda^{-1} - \lambda^2 + 3 - \lambda^{-1}\overline{\tau}^2}{J_m - 2\lambda^{-1} - \lambda^2 + 3}\right) + \frac{J_m\lambda^{-1}}{2} + \overline{\sigma}_o\lambda^{-1/2} + \overline{\mu}_s(2\lambda - \lambda^{-1} - \lambda^{-2} - \lambda^{-2}\overline{\tau}^2) + \frac{\overline{\lambda}_s}{2}\lambda^{-1}\log\lambda, \tag{18}$$

$$\frac{\overline{M}_z}{\pi} = \frac{J_m\lambda(J_m - 2\lambda^{-1} - \lambda^2 + 3)}{\overline{\tau}^3}\log\left(\frac{J_m - 2\lambda^{-1} - \lambda^2 + 3}{J_m - 2\lambda^{-1} - \lambda^2 + 3 - \lambda^{-1}\overline{\tau}^2}\right) - \frac{J_m}{\overline{\tau}} + 2\overline{\mu}_s\lambda^{-1}\overline{\tau}. \tag{19}$$

B. Simple torsion and pure extension

In special case of simple torsion, the cylinder is held at $\lambda = 1$, while $\overline{\tau}$ is varied. In that case, the axial force and moments take the simple expressions

$$\frac{\overline{F}_z}{\pi} = -\frac{1}{4}\overline{\tau}^2 + \overline{\sigma}_o - \overline{\mu}_s\overline{\tau}^2,$$
$$\frac{\overline{M}_z}{\pi} = \left(\frac{1}{2} + 2\overline{\mu}_s\right)\overline{\tau}, \tag{20}$$

for a neo-Hookean solid, and

$$\frac{\overline{F}_z}{\pi} = \frac{J_m^2}{2\overline{\tau}^2}\log\left(\frac{J_m - \overline{\tau}^2}{J_m}\right) + \frac{J_m}{2} + \overline{\sigma}_o - \overline{\mu}_s\overline{\tau}^2,$$
$$\frac{\overline{M}_z}{\pi} = \frac{J_m^2}{\overline{\tau}^3}\log\left(\frac{J_m}{J_m - \overline{\tau}^2}\right) - \frac{J_m}{\overline{\tau}} + 2\overline{\mu}_s\overline{\tau}, \tag{21}$$

for one that obeys the Gent model. Note that in either case, the expression for the torque contains only $\overline{\mu}_s$. The axial force in pure torsion is not zero and its surface contribution part depends on $\overline{\sigma}_o$ and $\overline{\mu}_s$. The constant $\overline{\lambda}_s$ does not enter Eqs. (20) or (21).

In case of pure extension (compression), when $\overline{\tau} = 0$, and λ is varied, $\overline{M}_z = 0$. For the neo-Hookean solid,

$$\frac{\overline{F}_z}{\pi} = (\lambda - \lambda^{-2}) + \overline{\sigma}_o\lambda^{-1/2} + \overline{\mu}_s(2\lambda - \lambda^{-1} - \lambda^{-2}) + \frac{\overline{\lambda}_s}{2}\lambda^{-1}\log\lambda, \tag{22}$$

and for solids obeying the Gent model,

$$\frac{\overline{F}_z}{\pi} = \frac{J_m(\lambda - \lambda^{-2})}{J_m - 2\lambda^{-1} - \lambda^2 + 3} + \overline{\sigma}_o\lambda^{-1/2} + \overline{\mu}_s(2\lambda - \lambda^{-1} - \lambda^{-2}) + \frac{\overline{\lambda}_s}{2}\lambda^{-1}\log\lambda. \tag{23}$$

In pure extension (compression), the axial force depends on all three constants associated with surface hyperelasticity.

The three constants $\overline{\sigma}_o$, $\overline{\mu}_s$, and $\overline{\lambda}_s$ can be determined through the following deformation sequence:

(1) At $\lambda = 1$, right after the mold is removed [see Fig. 1(b)], $\overline{F}_z(1) \neq 0$. The upper plate experiences a force $\overline{F}_z = \pi\overline{\sigma}_o$. Therefore, the parameter $\overline{\sigma}_o$ can be determined by measuring $\overline{F}_z(\lambda = 1)$.

(2) Further, a twist $\overline{\tau}L$ applied to the upper plate requires an axial torque M_z that depends only on $\overline{\mu}_s$. So, if the torque-twist response is available, $\overline{\mu}_s$ can be determined.

(3) Finally, using the axial force-extension (force-compression) response, the remaining constant $\overline{\lambda}_s$ can be determined.

Obviously, the forces and moments involved are small. For instance, when $\sigma_o \simeq 20$ mNm^{-1}, and $\mu_s \simeq 100$ mN m^{-1} (using typical values reported in Ref. [22]), the force at $\lambda = 1$ is of the order of ~ 10 μN for a cylinder of radius $R_0 = 100$ μm. Similarly, for a twist per unit length of $\tau = 1$ rad, the moments will be of the order of $\sim 10^4$ μN-μm. Using larger values of R_0 will increase the total force and moment but, according to Eqs. (20)–(23), the terms due to bulk deformation will overwhelm the surface hyperelastic terms.

The above procedure works if, as assumed in the derivations, the cylinder remains a cylinder throughout the deformation. Consequently, the expressions for axial force and moment, in either case, do not depend on the length L of the cylinder. Deviations from the ideal situation will lead to dependence on the length, as will be demonstrated in the next section.

Equations for F_z and M_z [Eqs. (20) and (21)] in pure torsion and for F_z in pure extension (compression) [Eqs. (22) and (23)] can be plotted for both neo-Hookean and Gent cases. In Figs. 3(a)–3(c), we plot only the bulk contributions to the forces and moments (i.e., in the case where $\sigma_o = \mu_s = \lambda_s = 0$). These plots indicate the sensitivity of the responses to the value of J_m. While a Gent hyperelastic material offers

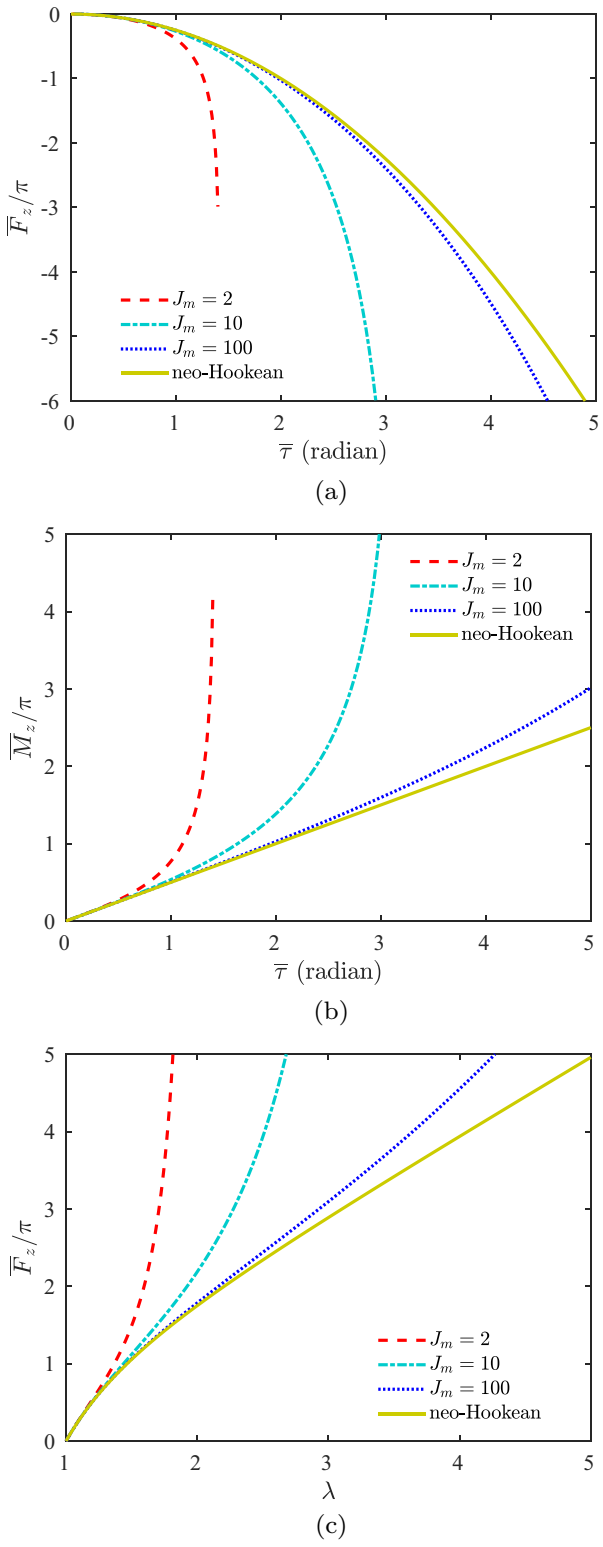

FIG. 3. Effect of the parameter J_m on (a) axial force-twist and (b) torque-twist responses in case of simple torsion and (c) force-extension response in case of uniaxial tension of a cylinder. No surface effects are considered here.

more variety in the hyperelastic response, for $J_m > 100$, the neo-Hookean and Gent materials have indistinguishable responses. For smaller values of J_m too, if the twist per unit nondimensionalized length is limited to about 1 rad and the axial stretch to about 1.5, the responses for both cases, for all values of J_m, are close. Thus for $\overline{\tau} < 1$ rad and $\overline{L} < 1.5$, the neo-Hookean model is adequate for the bulk.

III. RESULTS: POSSIBLE DEVIATIONS FROM THE IDEAL

The analytical closed-forms of the torque-twist, force-twist, and force-extension (force-compression) responses discussed in the previous section assume that the cylinder remains a cylinder all through the deformation. As mentioned earlier, a consequence of this is that the analytical responses are independent of the length L.

In this section, we compare the results from the closed-form response equations with FE solutions and attempt to identify limits within which the deformations must be performed in order that deviations from cylindricity are inconsequential.

Finite-element simulations are performed in the commercial software ABAQUS, using a user-defined element subroutine (UEL). The formulation for this UEL is discussed in detail in Ref. [28]. The UEL was developed for eight-noded surface elements, which are wrapped around the cylinder. The bulk is discretized with C3D20 and C3D15 for compressible cases and corresponding hybrid elements are used for incompressible. In case of extension (compression), we take advantage of the axisymmetry and use CAX8H elements for the bulk and a specially developed three-noded element for the surface. Details of the finite-element formulation are given in the Supplemental Material [30].

We consider four possible deviations from the ideal situation. In each case, we look at aspect ratios $\overline{L} = 1$ (which we call the short cylinder) and 5 or 10 (long cylinder).

(1) *Effect of bulk compressibility*. In the closed-form solutions derived, we have assumed the bulk to be incompressible, i.e., the bulk modulus $\kappa \to \infty$. A finite bulk modulus will affect the force-twist, torque-twist, and force-extension (force-compression) responses. Limits of $\overline{\kappa} = \kappa/\mu$, for which the closed-forms are useful, need to be established.

(2) *Effect of friction between the cylinder and the plates*. As shown in Fig. 4(a), the top and bottom surfaces of the cylinder may not be able to slip unhindered on the confining plates. In simple torsion, in particular, boundary conditions applied at the top and bottom are $(\theta - \Theta)|_0 = 0$ and $(\theta - \Theta)|_L = \tau L$. An extreme case is that of perfect stick where $r|_{0,L} = R$. On the contrary, perfect slip requires that $r|_{0,L}$ be completely unconstrained. To study the effect of friction between the soft solid and the constraining plates, we simulate the cases of perfect slip and perfect stick.

(3) *Effect of surface energy of the plates*. When the mold is removed, the cylinder is assumed to remain a cylinder. However, when the surface energies of the wall-air and wall-solid interfaces γ_{wa} and γ_{ws} are considered and perfect slip is allowed at $Z = 0$ and L, the cylindrical capillary bridge develops a meniscus as shown in Fig. 4(b), with the contact angle θ_c given by the Young's relation $\sigma_o \cos\theta_c = \gamma_{wa} - \gamma_{ws}$. Young's equation strictly holds when surface hyperelasticity is absent. The contact angle will deviate from θ_c when $\overline{\mu}_s$ and $\overline{\lambda}_s$ are not zero [28]. Torque-twist and force-twist responses of the noncylindrical capillary bridge should lead to responses that deviate from the ideal.

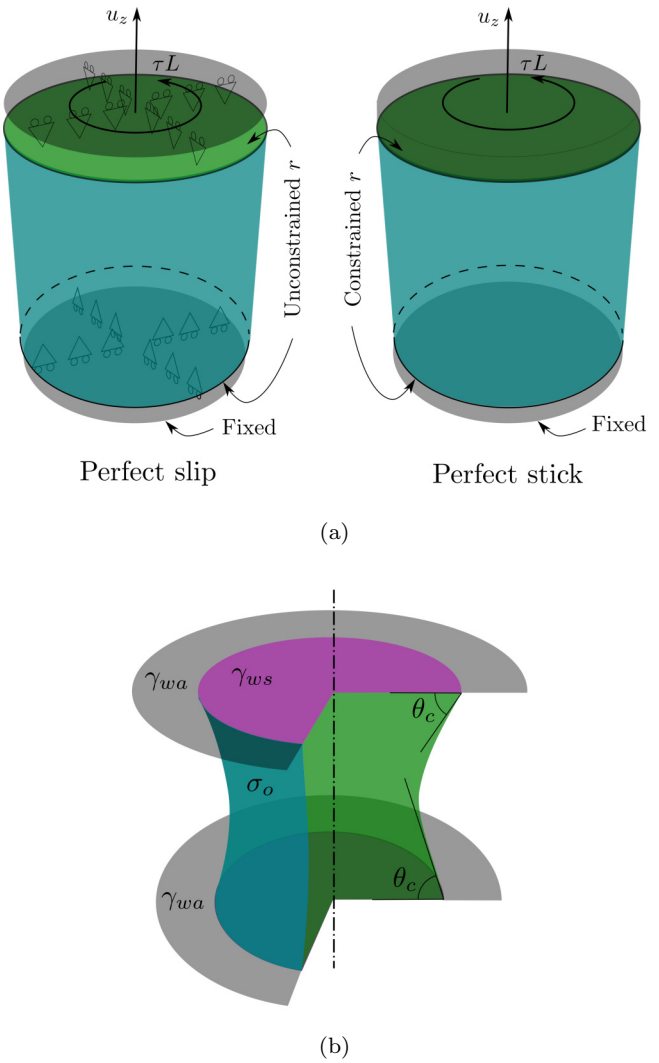

FIG. 4. "Perfect slip" and "perfect stick" boundary conditions are explained in (a). The cylinder develops into a meniscus (b) when perfect slip is allowed, and wall-air and wall-solid interface energies γ_{wa} and γ_{ws}, respectively, are considered.

(4) *Nonmonotonic force-extension behavior in uniaxial tension*. The force obtained in Eq. (22) for the neo-Hookean case, for certain combinations of surface parameters, may not be monotonically increasing with λ. As reported by Xuan and Biggins [31], the Rayleigh-Plateau instability ensues when the force-stretch curve is nonmonotonic. We consider cases where $\overline{\sigma}_o, \overline{\mu}_s, \overline{\lambda}_s \geqslant 0$. The axial force F_z is monotonically increasing if, for all values of λ, $\frac{d\overline{F}_z}{d\lambda} > 0$, which implies that

$$2\lambda^{3/2} + 4\lambda^{-3/2} - \overline{\sigma}_o + \overline{\mu}_s(4\lambda^{3/2} + 4\lambda^{-3/2} + 2\lambda^{-1/2}) + \overline{\lambda}_s\lambda^{-1/2}(1 - \log\lambda) > 0. \quad (24)$$

Clearly, any positive value of $\overline{\mu}_s$ will satisfy the above inequality. Thus, for a given value of $\overline{\mu}_s \geqslant 0$, it is possible to determine the region in the $\overline{\sigma}_o$-$\overline{\lambda}_s$ plane where the above inequality holds and therefore F_z increases monotonically with λ. For three values of $\overline{\mu}_s$, the domains in which $\overline{\sigma}_o$ and $\overline{\lambda}_s$ must lie in order that the force-extension response is monotonically increasing is shown in Fig. 5(a). The corresponding

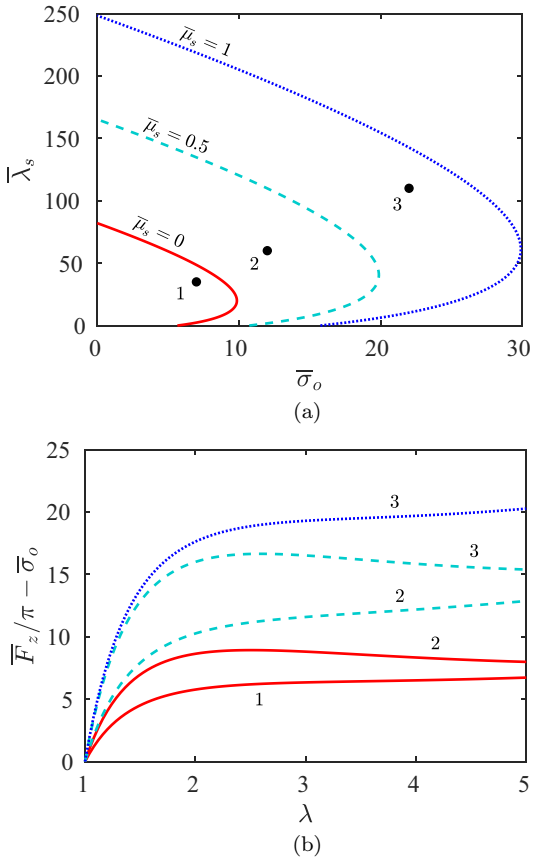

FIG. 5. (a) Bounds on surface parameters $\overline{\sigma}_o$ and $\overline{\lambda}_s$, for three values of $\overline{\mu}_s$, obtained from inequality (24). For a given $\overline{\mu}_s$, values of $\overline{\sigma}_o$ and $\overline{\lambda}_s$ lying to the left of the curve yield a monotonic force-stretch response. (b) Typical force-stretch responses in tension for parameters corresponding to points 1, 2, and 3 marked in (a).

force-extension responses are depicted in Fig. 5(b). For the three representative points marked 1, 2, and 3 in Fig. 5(a), the responses are shown for values of $\overline{\mu}_s$ to the left and right of the marked points. For example, for point 2, responses are plotted for $\overline{\mu}_s = 0$ [for which the parameters represented by point 2 do not satisfy inequality (24) and the response is not monotonically increasing] and $\overline{\mu}_s = 0.5$ (for which the monotonically increasing response is expected).

If the combination of surface parameters is such that a monotonically increasing response is expected, the cylinder should remain a cylinder throughout the deformation. However, constrained radial displacements at the wall-solid interface might change this situation. For the extreme cases with perfect slip and perfect stick at the interface, we explore the possibility of obtaining nonmonotonic force-extension responses even when the parameters $\overline{\sigma}_o, \overline{\mu}_s, \overline{\lambda}_s$ satisfy the inequality (24).

We will now explore the effects of the above deviations one by one. In all cases, results for the short cylinder ($\overline{L} = 1$) are plotted with thin lines and those for the long one ($\overline{L} = 5$ or 10) are plotted with thick lines. The bulk is assumed to obey neo-Hookean hyperelasticity for all cases reported henceforth.

The effect of compressibility, $\overline{\kappa} = \kappa/\mu$, is shown in Figs. 6(a) and 6(b) for the case of simple torsion. All cases

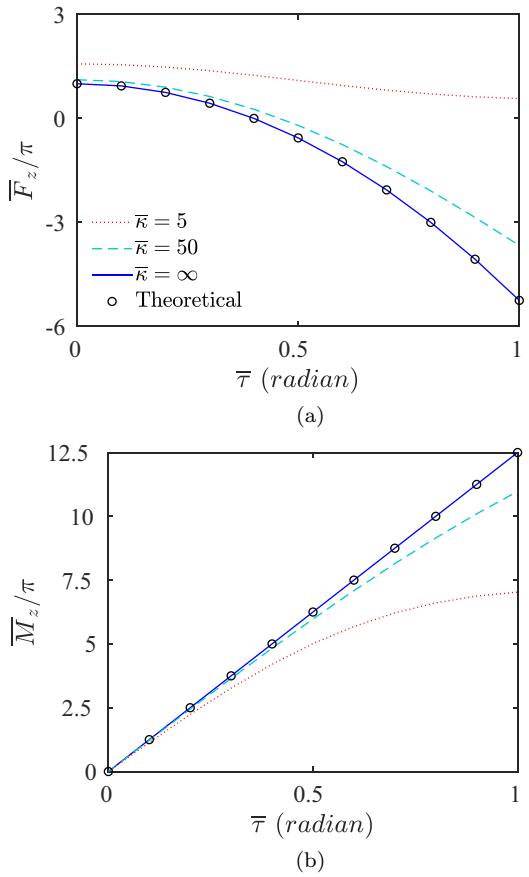

FIG. 6. Effect of normalized bulk modulus $\overline{\kappa} = \kappa/\mu$ on the (a) force-twist and (b) torque-twist responses in pure torsion. Perfect slip is assumed at the wall-solid interfaces. The bulk is assumed to be neo-Hookean. The results for the short and long cylinders are identical in this case and only one set is shown. Circles represent the closed-form expressions (20). The surface parameters taken are $\overline{\sigma}_o = 1$, $\overline{\mu}_s = 6$, and $\overline{\lambda}_s = 0$.

shown are for perfect slip at the wall. For all the cases simulated, both force-twist and torque-twist responses are independent of $\overline{L}$. As shown in Figs. 6(a) and 6(b), respectively, the closed-form expressions (20) expectedly match very well with the simulated response for the incompressible material. When the bulk is compressible, the response increasingly deviates from Eqs. (20). Even $F_z(\lambda = 1)$, from which $\overline{\sigma}_o$ is obtained, increases with compressibility. The torque-twist relation, shown in Fig. 6(b), is also sensitive to compressibility except for very small twist ($\overline{\tau} < 0.25$ rad). It is clear from Figs. 6(a) and 6(b) that the protocol for determining surface hyperelastic constants may not work if the bulk is highly compressible. The FE analyses in Fig. 6 show that, as a rule of thumb, limiting $\overline{\tau}$ to less than 0.25 rad will allow us to use the closed-form force-twist and torque-twist relations when the bulk modulus $\kappa \gtrsim 100\mu$.

In Fig. 7, results pertaining to perfect stick at the walls are presented. Under perfect stick, for compressible solids, the aspect ratio $\overline{L}$ affects both the force-twist and torque-twist responses shown in Figs. 7(a) and 7(b), respectively.

When the bulk is incompressible, for all values of $\overline{L}$, the responses match the theoretical ones. For moderate levels of compressibility ($\overline{\kappa} = 50$), longer cylinders remain closer to the theoretical force-twist response. The torque-twist response for compressible solids, on the other hand, is closer to the theoretical for shorter cylinders [see Fig. 7(b)]. As a compromise, by using $1 \leqslant \overline{L} \leqslant 5$, we can still utilize Eqs. (20) to extract the surface hyperelastic parameters, even when the bulk is moderately compressible. Equations (20) will not be applicable for highly compressible materials (e.g., $\overline{\kappa} = 5$).

The reason for dependence on the aspect ratio $\overline{L}$ in case of perfect stick at the walls is explained through Fig. 7(c). Here, deformed configurations of the cylinder at $\overline{\tau} = 1$ are shown. The deformed configurations are for a hyperelastic surface with strong dependence on surface strains. When the bulk is incompressible, both the short and long cylinders remain cylinders after deformation. But when the bulk is highly compressible and perfect stick conditions prevail at the wall-solid interface, the deformed configuration deviates from cylindricity. The responses, therefore, deviate from the theoretical and also exhibit dependence on $\overline{L}$.

In case of uniaxial tension too, responses for the case of perfect slip at the wall-solid boundary do not exhibit any dependence on $\overline{L}$ and follow Eq. (22) very faithfully. The dependence on length manifests, as in the case of pure torsion, in perfect stick condition.

Consider surface hyperelasticity parameter sets for which a monotonically increasing force-extension response is expected. For instance, $\overline{\sigma}_o = 0$, $\overline{\mu}_s = 0$, with $\overline{\lambda}_s = 50$ [see Fig. 5(a)] is one such case, for which the force-extension curve is shown in Fig. 8(a). In this case, the response of longer cylinder with perfect stick condition at the wall-solid interface is close to that predicted by Eq. (22).

Though the responses are very close, the deforming long cylinder does not remain exactly a cylinder during extension. The deformed shape at $\lambda \simeq 2$ develops an interesting feature as shown in Fig. 9(a). The initially cylindrical tube develops a periodic variation of the radius in the z direction for $\overline{\sigma}_o = 0$, $\overline{\mu}_s = 0$, and $\overline{\lambda}_s = 50$. At the same level of stretch, the amplitude of the periodic undulation is higher when $\overline{\sigma}_o$ is increased, as shown for $\overline{\sigma}_o = 5$. When this deformation is unstable, it will quickly lead to fracture of the cylinder. So, for practical purposes, uniaxial extension of long cylinders may not be feasible.

For short cylinder, on the other hand, the response is very far from ideal and also exhibits nonmonotonic behavior for the same set of parameters. As shown in Fig. 9(b), necking in the short cylinder due to expansion is severe and develops early in the deformation. The severe departure from cylindricity, into a capillary shape with a meniscus like a catenoid, causes the force-extension curve to be nonmonotonic.

The force-extension response is not always nonmonotonic, though it is always higher than that of the long cylinder. Nonmonotonicity is the result of high values of $\overline{\sigma}_o$ [as shown in Fig. 8(b)] or $\overline{\lambda}_s$ [as shown in Fig. 8(a)]. High values of $\overline{\mu}_s$, on the other hand, restore the monotonic behavior [as shown in Fig. 8(c)] and suppress the instability [as shown in Fig. 9(a)].

Finally, we consider the case where perfect slip prevails at the wall-solid interface but balance of forces at the contact line lead to a contact angle $\theta_c \neq \pi/2$. The effect of surface hyperelasticity on the actual value of θ_c that the undeformed

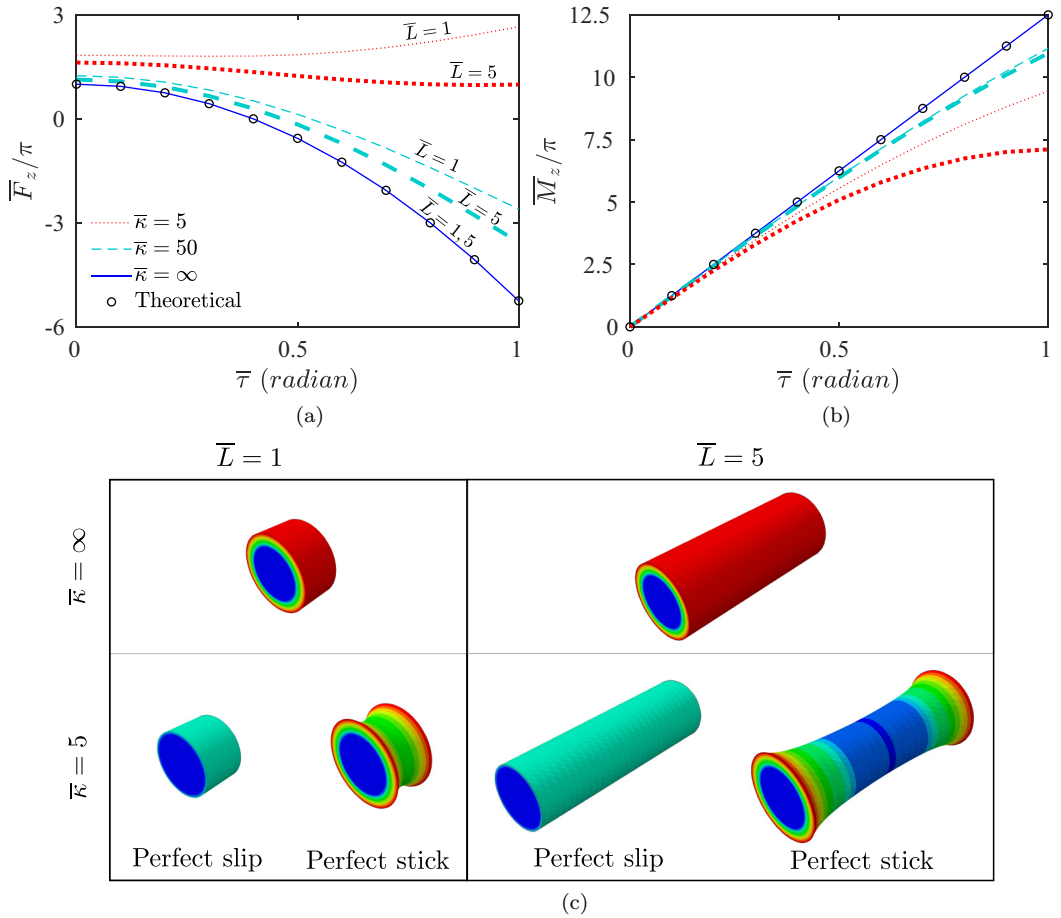

FIG. 7. (a) Force-twist and (b) torque-twist responses of long ($\overline{L}=5$, thick curves) and short ($\overline{L}=1$, thin curves) cylinders under the condition of perfect stick at the walls. The three colors (line styles) represent three values of $\overline{\kappa}=5$, 50, and ∞. Responses using the closed-form expressions in Eqs. (20) have been shown by circles. The values of surface properties considered here are $\overline{\sigma}_o=1$, $\overline{\mu}_s=6$, and $\overline{\lambda}_s=0$. Deformed shapes at $\overline{\tau}=1$ are shown in (c) for long and short cylinders. The top row is for cases where the bulk is incompressible and the bottom one is for highly compressible. Deformed configurations with both perfect slip and perfect stick are shown for the compressible case.

cylinder adopts is discussed in detail in Ref. [28]. In particular, the meniscus shape developed by the solid capillary bridge has been compared to a similar liquid bridge. Unless $\overline{\sigma}_o$ is very high, the solid bridge does not adopt a shape that has constant mean curvature like a liquid bridge. When extended uniaxially, the solid bridge attains a shape with constant mean curvature. The value of which is not governed merely by $\overline{\sigma}_o$ but also depends on $\overline{\mu}_s$ and $\overline{\lambda}_s$.

We consider a surface that is strongly sensitive to surface strains. When θ_c in the initial configuration is 90°, i.e., $\gamma_{ws}=\gamma_{wa}$, there is no effect of length on the force-twist or torque-twist response. In fact, as shown in Fig. 10(b), the torque-twist response is remarkably independent of θ_c.

However, the force-twist response is affected significantly by θ_c. When $\theta_c\neq 90°$, a sharp change in curvature develops close to the contact line [see the deformed configuration in Fig. 10(c) at $\overline{\tau}=0.4$ rad] in order to satisfy the Young's equation there. For short cylinders, the region of high curvature is a significant part of the total length. As shown in Fig. 10(a), for $\theta_c=30°$ and 60°, the force-twist response for $\overline{L}=1$ deviates significantly from the theoretical. For $\overline{L}=5$, the region of high curvature is a small part of the total length and over rest of the length, cylindricity is maintained. As a result, the force-twist response for $\overline{L}=5$ deviates only slightly from the theoretical [see Fig. 10(a)].

IV. CONCLUSIONS

Equations (20) and (22), for a bulk obeying neo-Hookean hyperelastic model, and (21) and (23), for the Gent model, demonstrate the theoretical possibility of determining surface hyperelastic parameters through a set of pure torsion and pure extension (compression) tests on a soft solid cylinder.

We consider a model of surface hyperelasticity characterized by three parameters. The parameter $\overline{\sigma}_o$ is associated with the part of the Cauchy surface stress that is independent of surface strains. The parameters $\overline{\mu}_s$ and $\overline{\lambda}_s$ govern the response of the surface to surface strains. The parameter $\overline{\mu}_s$ can be obtained from the torque-twist response, $\overline{\sigma}_o$ from the axial force at zero twist, while $\overline{\lambda}_s$ can be obtained from a force-extension (force-compression) response.

The equations are exact for a cylinder held between two confining plates, with an incompressible bulk, perfect slip conditions at the wall-solid interface, and very low surface energies of the confining plates as well as the wall-solid

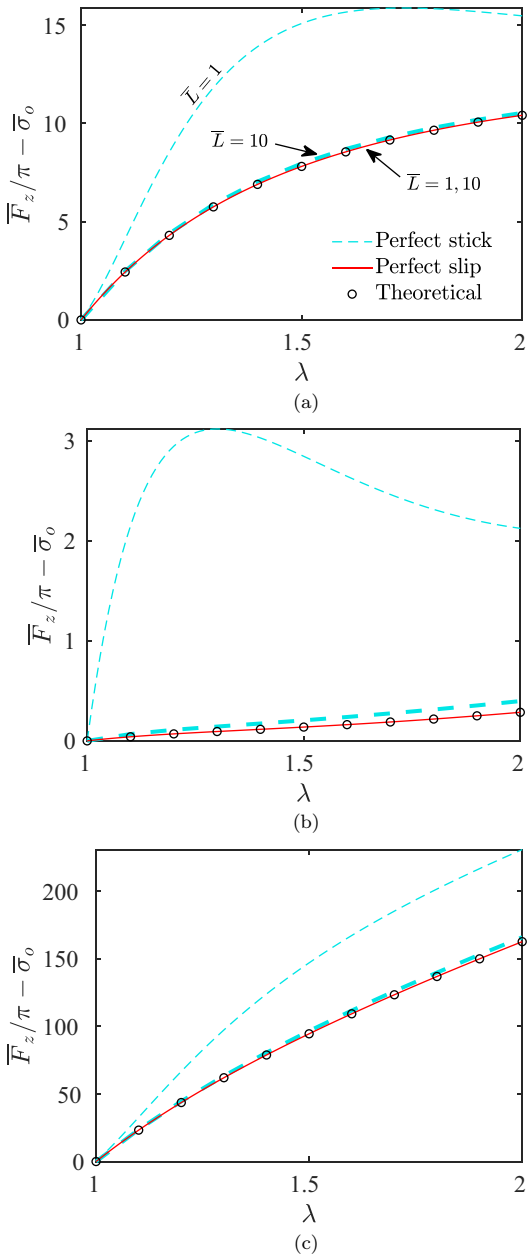

FIG. 8. Force-extension responses of short ($\overline{L}=1$, thin lines) and long cylinders ($\overline{L}=10$, thick lines) in perfect slip and perfect stick conditions at the wall-solid interface for (a) $\overline{\sigma}_o=0$, $\overline{\mu}_s=0$, and $\overline{\lambda}_s=50$, (b) $\overline{\sigma}_o=5$, $\overline{\mu}_s=0$, and $\overline{\lambda}_s=0$, and (c) $\overline{\sigma}_o=5$, $\overline{\mu}_s=50$, and $\overline{\lambda}_s=0$. For perfect slip, the responses of the short and long cylinders are closely identical and the responses only for $\overline{L}=1$ are shown. Circles represent the closed-form expression (22). In case of perfect stick condition, the responses of the long and short cylinders are very different.

interface. Moreover, it is assumed that the cylinder remains a cylinder all through the deformation.

Possible deviations from ideal situations assumed in deriving these equations are explained through numerical simulations. The simulations indicate the following:

(1) Actual responses are close to theoretical ones pertaining to a neo-Hookean bulk when deformations imparted are small ($\overline{\tau}<1$, $\lambda<1.5$). When they are large, finite extensibility of the bulk is expected to play a role and the Gent model with an appropriate value of J_m must be used (Fig. 3).

(2) Theoretical responses are strictly valid for incompressible bulk but continue to hold if the bulk modulus $\kappa \geqslant 100\mu$ (Fig. 6).

(3) Deviations from theoretical expectations arise when there is significant friction at the wall-solid interfaces, especially when the bulk is compressible. Nearly incompressible solids with an aspect ratio (ratio of length to radius) of the sample of about 5 exhibit force-twist and torque-twist responses reasonably close to the theoretical (Fig. 7).

(4) Force-extension (force-compression) responses predicted by Eqs. (22) and (23) remain valid only if friction is absent at the wall-solid interface (Fig. 9).

(5) Deviations from cylindricity of the sample occur when the contact angle at the wall-solid contact line is different than 90°. Samples with an aspect ratio $\simeq$5 minimize the effects of strong changes in curvature in the vicinity of the contact line (Fig. 10).

Finally, it is interesting to estimate the range of forces and torques that need to be measured and sample sizes that must be used to realize this theoretical possibility. These can be roughly assessed by considering a real material that has $\mu=3$ kPa, $\sigma_o=20$ mN m^{-1}, $\mu_s=100$ mN m^{-1}, and $\lambda_s=0$ mN m^{-1}. These values are in the range of those calculated by Xu *et al.* [32] for silicone gels.

Assuming these values, and the fact that incompressibility of the bulk and restrictions on the sample's aspect ratio are met, the force-twist, torque-twist, and force-extension relations are shown in Figs. 11(a)–11(c) for various values of the radius R_0. As R_0 varies from 50 to 10 000 μm, the nondimensional parameters $\overline{\sigma}_o$ and $\overline{\mu}_s$ vary from 0.13 to 6.7×10^{-4} and 0.67 to 3.33×10^{-3}, respectively.

The behavior of the torque-twist relation in Fig. 11(b) is rather straightforward. As long as $\overline{\mu}_s$ is comparable to 0.5 [see Eq. (20)], the slope changes appreciably with radius. When R_0 is large (i.e., $\overline{\mu}_s$ is small), the torque-twist response of the cylinder is overwhelmingly dominated by the bulk. For $R_0=50$ and 200 μm ($\overline{\mu}_s=0.67$ and 0.17, respectively), the slope of the torque-twist response changes with $\overline{\mu}_s$. For higher R_0, it does not. The order of the torque that needs to be measured for $R_0=50$ μm is 2000 μN-μm. Also, at $R_0=50$ μm, to determine σ_o, $F_z(\lambda=1)\simeq\pi$ μN.

The force-twist and force-extension responses [shown in Figs. 11(a) and 11(c), respectively] behave in the same way. Above $R_0\sim200$ μm, the response changes imperceptibly with $\overline{\mu}_s$, since an overwhelmingly large part of the force is borne by the bulk. For $R_0<200$ μm, the surface parameters have a significant effect on the response.

For this particular example, the force-extension curve is not required as $\lambda_s=0$. However, the level of force to be measured during extension (compression) is of the order of 100 μN for $R_0=50$ μm.

Soft solids with stiffnesses in the range of 1–1000 kPa are increasingly being used in applications ranging from novel adhesives and soft robotics, to tissue engineering [33–35]. There is also an increasingly convincing body of evidence that points to the fact that many of these materials exhibit strong surface elasticity.

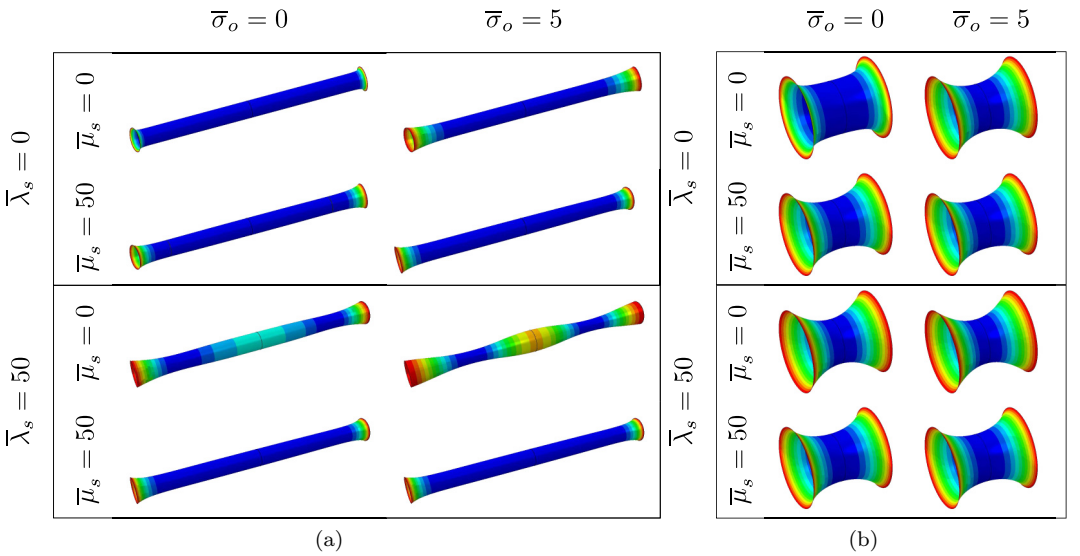

FIG. 9. Deformed configurations of a soft solid cylinder under extension at $\lambda = 2$, for lengths (a) $\overline{L} = 10$ and (b) $\overline{L} = 1$. The configurations are shown for various values of the surface parameters.

The ability to modulate surface stresses by varying the extent of surface strain opens up interesting technological possibilities. For instance, the ability to control capillary forces arising from tunable surface stresses can be useful in many applications in soft robotics [36]. In biological systems, understanding how surface stresses influence tissue shape and growth kinetics may lead to a better understanding of signaling between cells and their mechanical environment [37]. Active modulation of interfacial stresses between cells may be responsible for the differentiation of tissues at early stages

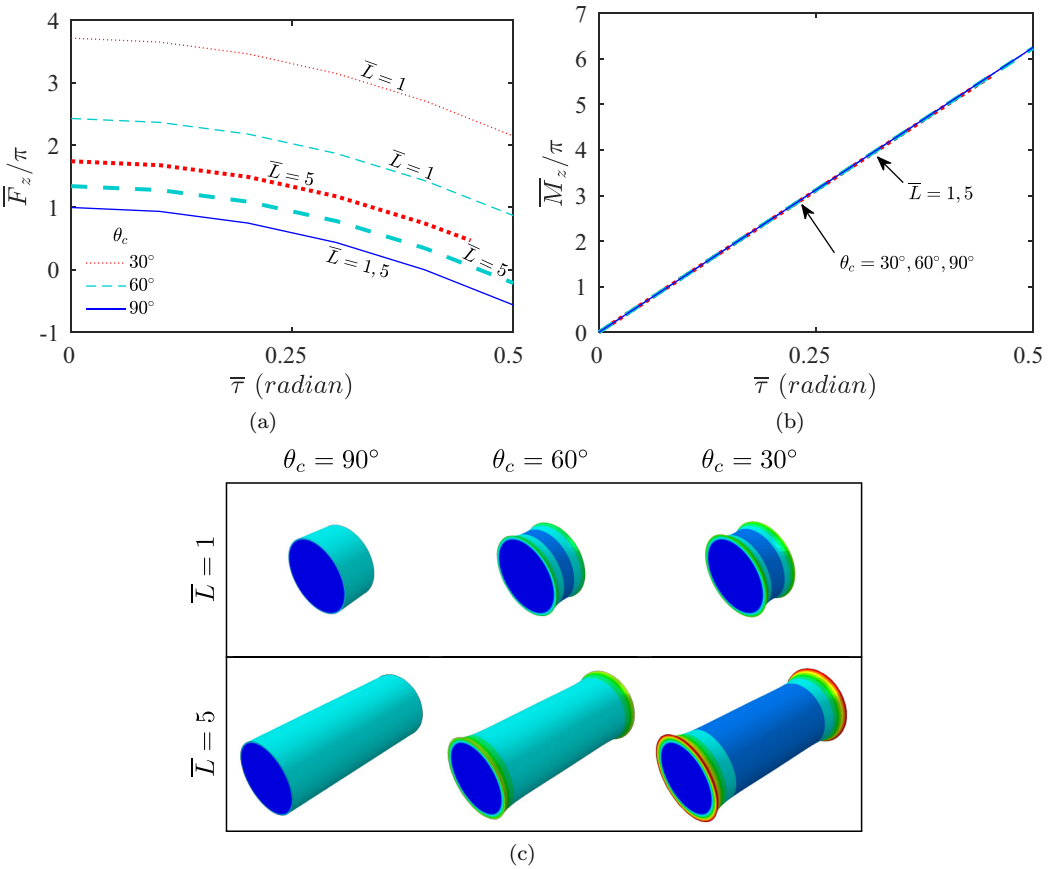

FIG. 10. (a) Force-twist and (b) torque-twist responses of cylinders with an initial aspect ratio $\overline{L} = 1$ (thin lines) and 5 (thick lines) for three different values of θ_c. The configurations at $\overline{\tau} = 0.4$ rad are shown for these values of the initial contact angle in (c).

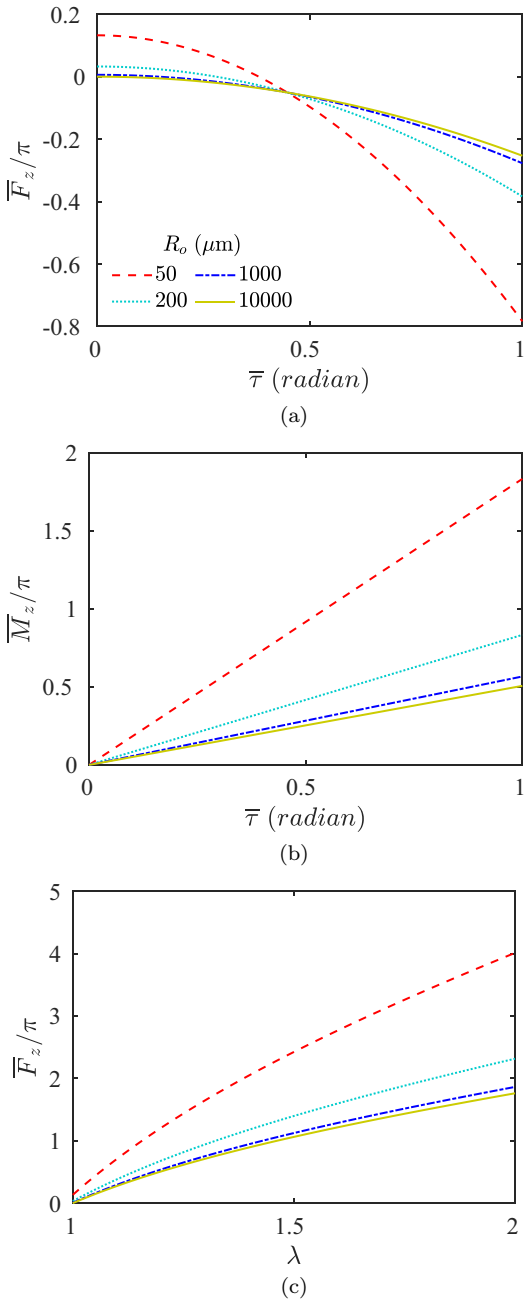

FIG. 11. Ideal (a) force-twist and (b) torque-twist and (c) force-extension responses of a real material with bulk shear modulus $\mu = 3$ kPa and surface hyperelastic properties given by $\sigma_o = 20$, $\mu_s = 100$, and $\lambda_s = 0$ mN m^{-1}, for initial radii $R_0 = 50$, 200, 1000, and 10 000 μm. The corresponding nondimensional surface parameters are $\overline{\sigma}_o = 0.13, 0.03, 0.007, 0.0007$, and $\overline{\mu}_s = 0.67, 0.17, 0.03, 0.003$.

of embryonic development [38]. The ability to accurately characterize and parametrize surface constitutive models for these materials is essential for modeling their mechanics of deformation. Especially on the scale of micrometers, it is often not possible to neglect the effect of surface stresses in these materials.

Calibrating surface constitutive behavior is challenging because of the smallness of the test samples, difficulties associated with handling them, and the extremely small forces and displacements that need to be sensitively measured. However, the development of direct or indirect protocols for obtaining surface structure-property relationships for these materials is imperative for designing and understanding practical systems.

APPENDIX A: CONSEQUENCES OF INCOMPRESSIBILITY OF THE BULK

The equilibrium equation [Eq. (1)] can be written in terms of the bulk Cauchy stress components as

$$\sigma_{rr,r} + \frac{\sigma_{rr} - \sigma_{\theta\theta}}{r} = 0,$$
$$\frac{1}{r}\sigma_{\theta\theta,\theta} + \sigma_{\theta z,z} = 0,$$
$$\frac{1}{r}\sigma_{\theta z,\theta} + \sigma_{zz,z} = 0, \tag{A1}$$

which leads to equations for the pressure $p(r, \theta, z)$,

$$p_{,r} = -2W_1\tau^2 r + (2W_1\lambda^{-1} - 2W_2\lambda)_{,r}, \quad p_{,\theta} = 0 \quad p_{,z} = 0, \tag{A2}$$

which show that p is a function of r only. By integrating the first of the above equations, we get

$$p = -\int 2W_1\tau^2 r dr + (2W_1\lambda^{-1} - 2W_2\lambda) + C, \tag{A3}$$

where C is a constant of integration.

APPENDIX B: DERIVATION OF BULK AND SURFACE CAUCHY STRESS TENSORS $\boldsymbol{\sigma}$ AND $\boldsymbol{\sigma}^s$

A body deforms from a reference configuration to a current configuration such that a material point $\boldsymbol{X} = R\boldsymbol{E}_R + Z\boldsymbol{E}_Z$ in the reference configuration maps to a point $\boldsymbol{x} = r\boldsymbol{e}_r + z\boldsymbol{e}_z$ in the current configuration. The deformation gradient tensor is defined as $\boldsymbol{F} = \nabla_0 \boldsymbol{x}$, where $\nabla_0 = \frac{\partial}{\partial R}\boldsymbol{E}_R + \frac{\partial}{R\partial\Theta}\boldsymbol{E}_\Theta + \frac{\partial}{\partial Z}\boldsymbol{E}_Z$ is the gradient operator in the reference cylindrical coordinate system. Now, using the chain rule of differentiation,

$$\begin{aligned}\boldsymbol{F} = {} & r_{,R}\boldsymbol{e}_r \otimes \boldsymbol{E}_R + \frac{r_{,\Theta}}{R}\boldsymbol{e}_r \otimes \boldsymbol{E}_\Theta + r_{,Z}\boldsymbol{e}_r \otimes \boldsymbol{E}_Z \\ & + \theta_{,R} r\boldsymbol{e}_\theta \otimes \boldsymbol{E}_R + \theta_{,\Theta}\frac{r}{R}\boldsymbol{e}_\theta \otimes \boldsymbol{E}_\Theta + \theta_{,Z} r\boldsymbol{e}_\theta \otimes \boldsymbol{E}_Z \\ & + z_{,R}\boldsymbol{e}_z \otimes \boldsymbol{E}_R + \frac{z_{,\Theta}}{R}\boldsymbol{e}_z \otimes \boldsymbol{E}_\Theta + z_{,Z}\boldsymbol{e}_z \otimes \boldsymbol{E}_Z,\end{aligned} \tag{B1}$$

which can be further simplified for the motion shown in Fig. 2. Using the motion described by Eq. (3), we have, in matrix form,

$$\boldsymbol{F} = \begin{pmatrix} \lambda^{-1/2} & 0 & 0 \\ 0 & \lambda^{-1/2} & \tau r \\ 0 & 0 & \lambda \end{pmatrix}. \tag{B2}$$

The Cauchy stress tensor for incompressible bulk is given as [39]

$$\boldsymbol{\sigma} = -p(r, \theta, z)\mathbf{1} + 2W_1\boldsymbol{B} - 2W_2\boldsymbol{B}^{-1}, \tag{B3}$$

where $W_1 = \frac{\partial W}{\partial I_1}$ and $W_2 = \frac{\partial W}{\partial I_2}$. Now using Eqs. (B2) and (B3) and the left Cauchy-Green strain $\boldsymbol{B} = \boldsymbol{F}\boldsymbol{F}^T$, it is easy to obtain Eq. (4).

Let us consider the lateral surface of the cylinder with normal $\boldsymbol{E}_R$ in the reference configuration at radial position R. The surface deformation gradient $\boldsymbol{F}^s$ [40] can be written in matrix notation as

$$\boldsymbol{F}^s = \begin{pmatrix} 0 & 0 \\ \lambda^{-1/2} & \tau r \\ 0 & \lambda \end{pmatrix}. \tag{B4}$$

Now using the expression of the Cauchy surface stress tensor [28]

$$\boldsymbol{\sigma}^s = \frac{1}{\sqrt{I_2^s}} \boldsymbol{F}^s \boldsymbol{T}^s (\boldsymbol{F}^s)^T, \tag{B5}$$

where

$$\boldsymbol{T}^s = 2\gamma_1 \mathbf{1}_X + 2\gamma_2 I_2^s (\boldsymbol{C}^s)^{-1}, \tag{B6}$$

we obtain Eq. (6).

APPENDIX C: DETERMINING $\mathrm{div}^s\,\boldsymbol{\sigma}^s$ AND C

At the surface $r = r_0$, equilibrium is governed by Eq. (2) connecting the bulk Cauchy stress $\boldsymbol{\sigma}$ to $\boldsymbol{\sigma}^s$. In particular, the surface divergence of $\boldsymbol{\sigma}^s$ is defined as

$$\mathrm{div}^s \boldsymbol{\sigma}^s \cdot \boldsymbol{k} = \mathrm{div}^s[(\boldsymbol{\sigma}^s)^T \boldsymbol{k}^s], \tag{C1}$$

where $\boldsymbol{k}^s$ is the vector component of an arbitrary vector $\boldsymbol{k}$, on the tangent plane at $\boldsymbol{x}$ [40]. The tangent plane in this case is spanned by $\boldsymbol{e}_\theta, \boldsymbol{e}_z$. Let $(\boldsymbol{\sigma}^s)^T \boldsymbol{k}^s = \boldsymbol{t}$, i.e.,

$$\boldsymbol{t} = \begin{pmatrix} t_\theta \\ t_z \end{pmatrix} = \begin{pmatrix} \sigma^s_{\theta\theta} k_\theta + \sigma^s_{\theta z} k_z \\ \sigma^s_{\theta z} k_\theta + \sigma^s_{zz} k_z \end{pmatrix}. \tag{C2}$$

Now using the relation $\mathrm{div}^s \boldsymbol{t} = \mathrm{tr}\, D\boldsymbol{t}$ with $D\boldsymbol{t} = \boldsymbol{P}_x \nabla \boldsymbol{t} \boldsymbol{I}_x$ and

$$\nabla \boldsymbol{t} = \begin{pmatrix} t_{r,r} & \frac{t_{r,\theta} - t_\theta}{r} & t_{r,z} \\ t_{\theta,r} & \frac{t_{\theta,\theta} + t_r}{r} & t_{\theta,z} \\ t_{z,r} & \frac{t_{z,\theta}}{r} & t_{z,z} \end{pmatrix},$$

we obtain

$$\mathrm{div}^s[(\boldsymbol{\sigma}^s)^T \boldsymbol{k}^s] = \frac{\sigma^s_{\theta\theta,\theta} k_\theta + \sigma^s_{\theta z,\theta} k_z}{r} + \sigma^s_{\theta z,z} k_\theta + \sigma^s_{zz,z} k_z - \frac{\sigma^s_{\theta\theta} k_r}{r}. \tag{C3}$$

Here, $\boldsymbol{P}_x$ and $\boldsymbol{I}_x$ are the projection and inclusion maps at $\boldsymbol{x}$, respectively [40]. In the above, we have used the relations $k_{\theta,\theta} = -k_r$, $k_{\theta,z} = k_{z,\theta} = k_{z,z} = 0$. Now using the Eqs. (C1) and (C3), we obtain

$$\mathrm{div}^s \boldsymbol{\sigma}^s = -\frac{\sigma^s_{\theta\theta}}{r} \boldsymbol{e}_r + \left(\frac{\sigma^s_{\theta\theta,\theta}}{r} + \sigma^s_{\theta z,z} \right) \boldsymbol{e}_\theta + \left(\frac{\sigma^s_{\theta z,\theta}}{r} + \sigma^s_{zz,z} \right) \boldsymbol{e}_z. \tag{C4}$$

Since $\boldsymbol{\sigma}^s$ is independent of θ and z [see Eq. (6)], the above relation can be further simplified as

$$\mathrm{div}^s \boldsymbol{\sigma}^s = -\frac{\sigma^s_{\theta\theta}}{r} \boldsymbol{e}_r. \tag{C5}$$

Applying the boundary condition Eq. (2), we find that

$$p(r_0) = 2W_1(r_0)\lambda^{-1} - 2W_2(r_0)\lambda + \frac{2\gamma_1 \left(\lambda^{-3/2} + \lambda^{-1/2} \tau^2 r_0^2 \right) + 2\gamma_2 \lambda^{1/2}}{r_0}. \tag{C6}$$

Substituting the above into Eq. (A3), we can finally determine C as

$$C = \int 2W_1 \tau^2 r dr \Big|_{r_0} + \frac{2\gamma_1 \left(\lambda^{-3/2} + \lambda^{-1/2} \tau^2 r_0^2 \right) + 2\gamma_2 \lambda^{1/2}}{r_0}. \tag{C7}$$

[1] M. M. Nicolson, Surface tension in ionic crystals, Proc. R. Soc. London, Ser. A **228**, 490 (1955).

[2] R. Shuttleworth, The surface tension of solids, Proc. Phys. Soc. A **63**, 444 (1950).

[3] P. Sharma and S. Ganti, Size-dependent Eshelby's tensor for embedded nano-inclusions incorporating surface/interface energies, J. Appl. Mech. Trans. ASME **71**, 663 (2004).

[4] R. E. Miller and V. B. Shenoy, Size-dependent elastic properties of nanosized structural elements, Nanotechnology **11**, 139 (2000).

[5] H. Ahmadzadeh-Bakhshayesh, M. Y. Gutkin, and H. M. Shodja, Surface/interface effects on elastic behavior of a screw dislocation in an eccentric core–shell nanowire, Int. J. Solids Struct. **49**, 1665 (2012).

[6] R. W. Style, C. Hyland, R. Boltyanskiy, J. S. Wettlaufer, and E. R. Dufresne, Surface tension and contact with soft elastic solids, Nat. Commun. **4**, 2728 (2013).

[7] N. Nadermann, C. Y. Hui, and A. Jagota, Solid surface tension measured by a liquid drop under a solid film, Proc. Natl. Acad. Sci. U.S.A. **110**, 10541 (2013).

[8] S. J. Park, B. M. Weon, J. S. Lee, J. Lee, J. Kim, and J. H. Je, Visualization of asymmetric wetting ridges on soft solids with X-ray microscopy, Nat. Commun. **5**, 4369 (2014).

[9] S. Mondal, M. Phukan, and A. Ghatak, Estimation of solid-liquid interfacial tension using curved surface of a soft solid, Proc. Natl. Acad. Sci. U.S.A. **112**, 12563 (2015).

[10] X. Xu, A. Jagota, D. Paretkar, and C. Y. Hui, Surface tension measurement from the indentation of clamped thin films, Soft Matter **12**, 5121 (2016).

[11] A. Colas and J. Curtis, Silicones, in *Handbook of Polymer Applications in Medicine and Medical Devices* (Elsevier, Amsterdam, 2013), pp. 131–143.

[12] A. Nauta, B. Larson, M. T. Longaker, and H. Peter Lorenz, Scarless wound healing, in *Principles of Regenerative Medicine* (Elsevier, Amsterdam, 2011), pp. 103–127.

[13] W. Wang, R. Narain, and H. Zeng, Hydrogels, in *Polymer Science and Nanotechnology* (Elsevier, Amsterdam, 2020) pp. 203–244.

[14] C. Wong and R. Tummala, Polymers for electronic packaging in the 21st century, in *Applied Polymer Science: 21st Century* (Elsevier, Amsterdam, 2000) pp. 659–676.

[15] A. Chakrabarti, A. Porat, E. Raphael, T. Salez, and M. K. Chaudhury, Elastowetting of soft hydrogel spheres, Langmuir **34**, 3894 (2018).

[16] K. E. Jensen, R. W. Style, Q. Xu, and E. R. Dufresne, Strain-Dependent Solid Surface Stress and the Stiffness of Soft Contacts, Phys. Rev. X **7**, 041031 (2017).

[17] Z. Liu, K. E. Jensen, Q. Xu, R. W. Style, E. R. Dufresne, A. Jagota, and C.-Y. Hui, Effects of strain-dependent surface stress on the adhesive contact of a rigid sphere to a compliant substrate, Soft Matter **15**, 2223 (2019).

[18] J. T. Pham, F. Schellenberger, M. Kappl, and H.-J. Butt, From elasticity to capillarity in soft materials indentation, Phys. Rev. Materials **1**, 015602 (2017).

[19] S. Mora, T. Phou, J.-M. Fromental, L. M. Pismen, and Y. Pomeau, Capillarity Driven Instability of a Soft Solid, Phys. Rev. Lett. **105**, 214301 (2010).

[20] A. Chakrabarti and M. K. Chaudhury, Direct measurement of the surface tension of a soft elastic hydrogel: Exploration of elastocapillary instability in adhesion, Langmuir **29**, 6926 (2013).

[21] A. Javili and P. Steinmann, A finite element framework for continua with boundary energies. Part II: The three-dimensional case, Comput. Methods Appl. Mech. Eng. **199**, 755 (2010).

[22] Q. Xu, K. E. Jensen, R. Boltyanskiy, R. Sarfati, R. W. Style, and E. R. Dufresne, Direct measurement of strain-dependent solid surface stress, Nat. Commun. **8**, 555 (2017).

[23] D. J. Steigmann and R. W. Ogden, Elastic surface-substrate interactions, Proc. R. Soc. London, Ser. A **455**, 437 (1999).

[24] Z. P. Huang and J. Wang, A theory of hyperelasticity of multi-phase media with surface/interface energy effect, Acta Mech. **182**, 195 (2006).

[25] Z.-Q. Wang, Y.-P. Zhao, and Z.-P. Huang, The effects of surface tension on the elastic properties of nano structures, Int. J. Eng. Sci. **48**, 140 (2010).

[26] P. Chhapadia, P. Mohammadi, and P. Sharma, Curvature-dependent surface energy and implications for nanostructures, J. Mech. Phys. Solids **59**, 2103 (2011).

[27] S. Krichen, L. Liu, and P. Sharma, Liquid inclusions in soft materials: Capillary effect, mechanical stiffening and enhanced electromechanical response, J. Mech. Phys. Solids **127**, 332 (2019).

[28] M. R. Zafar and S. Basu, Axisymmetric capillary bridges of soft solids with surface elasticity, Mech. Mater. **155**, 103697 (2021).

[29] A. N. Gent, A new constitutive relation for rubber, Rubber Chem. Technol. **69**, 59 (1996).

[30] See Supplemental Material at http://link.aps.org/supplemental/10.1103/PhysRevE.103.063003 for the finite-element formulation of a hyperelastic surface.

[31] C. Xuan and J. Biggins, Plateau-Rayleigh instability in solids is a simple phase separation, Phys. Rev. E **95**, 053106 (2017).

[32] Q. Xu, R. W. Style, and E. R. Dufresne, Surface elastic constants of a soft solid, Soft Matter **14**, 916 (2018).

[33] C. Creton and E. Papon, Materials science of adhesives: How to bond things together, MRS Bull. **28**, 419 (2003).

[34] Y. Lee, W. Song, and J.-Y. Sun, Hydrogel soft robotics, Mater. Today Phys. **15**, 100258 (2020).

[35] J. L. Drury and D. J. Mooney, Hydrogels for tissue engineering: Scaffold design variables and applications, Biomaterials **24**, 4337 (2003).

[36] C. Majidi, Soft robotics: A perspective—Current trends and prospects for the future, Soft Robotics **1**, 5 (2013).

[37] S. Ehrig, B. Schamberger, C. M. Bidan, A. West, C. Jacobi, K. Lam, P. Kollmannsberger, A. Petersen, P. Tomancak, K. Kommareddy, F. D. Fischer, P. Fratzl, and J. W. C. Dunlop, Surface tension determines tissue shape and growth kinetics, Sci. Adv. **5**, eaav9394 (2019).

[38] F. Fagotto, The cellular basis of tissue separation, Development **141**, 3303 (2014).

[39] G. A. Holzapfel, *Nonlinear Solid Mechanics—A Continuum Approach for Engineering* (Wiley, Hoboken, NJ, 2000).

[40] M. E. Gurtin and A. I. Murdoch, A continuum theory of elastic material surfaces, Arch. Rat. Mech. Anal. **57**, 291 (1975).